Journal of Materials Chemistry A

PAPER

View Article Online
View Journal

Cite this: DOI: 10.1039/c7ta00413c

Kinetically controlled synthesis of two-dimensional Zr/Hf metal–organic framework nanosheets *via* a modulated hydrothermal approach†

Zhigang Hu,[a] Ezwan Mahmoud Mahdi,[b] Yongwu Peng,[a] Yuhong Qian,[a] Bin Zhang,[a] Ning Yan,[a] Daqiang Yuan,[c] Jin-Chong Tan[b] and Dan Zhao*[a]

The kinetically controlled synthesis of two-dimensional (2D) metal–organic framework (MOF) nanosheets in the absence of surfactants is rewarding but challenging. We herein describe such a surfactant-free bottom-up synthesis of 2D stable Zr/Hf MOF nanosheets named NUS-8 composed of $Zr_6O_4(OH)_4$ or $Hf_6O_4(OH)_4$ clusters and 1,3,5-benzenetribenzoate (BTB^{3-}) *via* a modulated hydrothermal approach, which allows fast precipitation and stabilization of intermediate 2D metal–organic nanosheets due to the heterogeneous synthetic conditions. Structural analyses based on synchrotron powder X-ray diffraction data confirm the 2D layered structure of NUS-8 with uniform porosity and highly accessible Lewis acid sites suitable for heterogeneous catalysis. 2D NUS-8 nanosheets exhibit excellent stabilities superior to those of their interlocked 3D MOF analogues synthesized from solvothermal synthesis, which are evidenced by comprehensive stability tests. In particular, dynamic mechanical analysis (DMA) experiments suggest that the stability of 2D NUS-8 nanosheets may come from a combination of interlayer shear sliding deformation and out-of-plane tension/compression modes whereas their interlocked 3D architecture is strictly constrained. Because of the alleviated framework strain and accessible active sites, NUS-8 nanosheets exhibit excellent stability and catalytic activity superior to those of their interlocked 3D MOF counterparts. Our work has demonstrated the potential of a modulated hydrothermal approach in the kinetically controlled synthesis of 2D MOF nanosheets, shedding light on future synthesis of 2D hybrid inorganic–organic materials.

Received 13th January 2017
Accepted 21st March 2017

DOI: 10.1039/c7ta00413c

rsc.li/materials-a

Introduction

Since the discovery of two dimensional (2D) graphene,[1] many 2D materials have been widely studied including hexagonal boron nitride (hBN), transition metal chalcogenides (TMCs, MoS_2), silicene, phosphorene, *etc.*,[2–5] which have exhibited unique anisotropic chemical, electronic, mechanical, and mass transport properties.[6,7] During the last two decades, metal–organic frameworks (MOFs) have become the frontier of crystalline porous materials and have been demonstrated with wide applications including gas storage, gas separation, heterogeneous catalysis, *etc.*[8–14] It is therefore of huge interest to explore 2D MOF nanosheets possessing readily accessible active sites, which may demonstrate novel properties in the applications of catalysis, electrochemistry, gas separation, *etc.*[15,16] Most of the reported 2D MOF nanosheets are based on the "top-down" exfoliation (*e.g.*, sonication and ball milling) of bulk MOFs with 2D layered structures.[17–20] However, the resultant products are often a mixture of nanosheets with wide distribution of thickness and lateral size, and are prone to degradation because of the strong mechanical force and harsh solvents required to overcome the interlayer interactions.[7] In this context, the alternative "bottom-up" strategy is more promising as it allows the direct growth of 2D MOF nanosheets with intact morphology and controlled thickness suitable for further applications.[21] The challenges for bottom-up strategies include undesirable interpenetration of individual layers and inherently strong interlayer-packing interactions stacking 2D layers into bulk materials for lower surface energy.[22] As a result, thermodynamically controlled approaches are often used involving surfactants, which can help to reduce the surface energy and thus to stabilize the resultant nanosheets.[23,24] Since surfactants may block the active sites should the nanosheets be used as catalysts, the complete removal of surfactants after their synthesis is necessary, which is however not so straightforward in most cases.[25] Therefore, the development of a surfactant-free bottom-up approach for the direct synthesis of 2D MOF

[a]Department of Chemical & Biomolecular Engineering, National University of Singapore, 117585, Singapore. E-mail: chezhao@nus.edu.sg

[b]Department of Engineering Science, University of Oxford, Parks Road, Oxford OX1 3PJ, UK

[c]State Key Laboratory of Structural Chemistry, Fujian Institute of Research on the Structure of Matter, Chinese Academy of Sciences, Fuzhou, 350002 Fujian, China

† Electronic supplementary information (ESI) available: Synthesis and characterization data. See DOI: 10.1039/c7ta00413c

nanosheets would be more appealing to facilitate both the synthetic procedures and purification processes, and more importantly to leave the active sites intact for catalytic applications.

In general, hydrothermal synthesis usually refers to heterogeneous reactions of crystal growth in aqueous media above 100 °C and 1 bar.[26] Currently, many MOFs are synthesized *via* this approach, such as MIL-101 and MIL-100.[27–29] However, in order to avoid the harsh synthetic conditions, the synthesis of MOFs under ambient conditions (near 100 °C and 1 bar) becomes prevailing and more promising for scale-up purposes nowadays.[30–33] In this work, we report a surfactant-free synthesis of 2D MOF nanosheets using a modulated hydrothermal approach (heterogeneous reactions in aqueous media near 100 °C and 1 bar) developed previously.[34–36] Because of the heterogeneous synthetic conditions, fast precipitation of intermediate products becomes possible, leading to kinetically controlled MOF products named NUS-8(Zr) and NUS-8(Hf) featuring 2D nanosheet morphology with a thickness of 10–20 nm and planar porous structures with highly exposed Lewis acid sites. NUS-8 nanosheets exhibit superior stability and catalytic activity over their interlocked 3D MOF analogues synthesized solvothermally.[37]

Results and discussion

Structural determination and morphology characterization

Traditional solvothermal synthesis using $ZrOCl_2 \cdot 8H_2O$ or $HfCl_4$ and 1,3,5-benzenetribenzoate acid (H_3BTB) in DMF/acetic acid solution resulted in a 3D structure [denoted as NUS-16(Zr/Hf) in this study for clarity],[37] arising from the interpenetration of 2D porous grids containing BTB^{3-} linked by 6-connected $Zr_6O_4(OH)_4$ clusters (Fig. 1, S1†). Interpenetration is a result of compensating the energy penalty by reaching a thermodynamically more stable state,[38] which is facilitated by the homogeneous synthetic condition for NUS-16. We hypothesize that heterogeneous synthetic conditions help avoid interpenetration by fast precipitation at high temperatures (120 °C) and stabilize intermediate 2D nanosheets affording kinetically controlled products. We successfully applied this modulated hydrothermal approach and obtained 2D layered MOF nanosheets, named NUS-8(Zr/Hf), which were subjected to synchrotron powder X-ray diffraction (PXRD) measurements for structural determination. Compared to the PXRD patterns of 3D NUS-16 (Fig. S1†), the peaks of crystal plane (220) representing the interpenetration structure are missing in the resultant NUS-8, strongly indicating the formation of 2D layered structures. Crystal models of NUS-8 featuring 2D layered structures were built based on the eclipsed stacking of monolayer grids from NUS-16 and refined by Rietveld refinement with acceptable accuracy *via* a LeBail route (Fig. 2). Taking NUS-8(Zr), for example, the crystal structure can be best described by eclipsed stacking of monolayers containing 3-connected BTB^{3-} ligands linked by 6-connected $Zr_6O_4(OH)_4$ clusters with a pore size of *ca.* 12.62 × 8.9 Å (Fig. 1). The calculated interlayer distances of NUS-8(Zr) and NUS-8(Hf) are 16.82 and 17.27 Å, respectively.[39] As seen from elemental analyses (Table S4†), the experimental metal to carbon weight ratio (0.87) is larger than the theoretical one (0.84), suggesting missing BTB^{3-} ligands in the structures (TGA results, ~0.07%). In order to prove that our modulated hydrothermal synthesis is kinetically controlled, we performed the experiments by putting 2D NUS-8 nanosheets in DMF/acetic solution at 120 °C for 24 h. We could not observe any transitions from 2D NUS-8 to 3D NUS-16 (Fig. S3†), confirming that 2D NUS-8 MOFs are kinetically controlled products.

The MOF morphology was examined by field-emission scanning electron microscopy (FE-SEM, Fig. 3a and d, S2†). Unlike the 3D interpenetrated NUS-16 crystals having rectangular brick shape (Fig. S2a and b†), NUS-8 MOFs exhibit nanosheet morphology, with a thickness of *ca.* 10–20 nm and

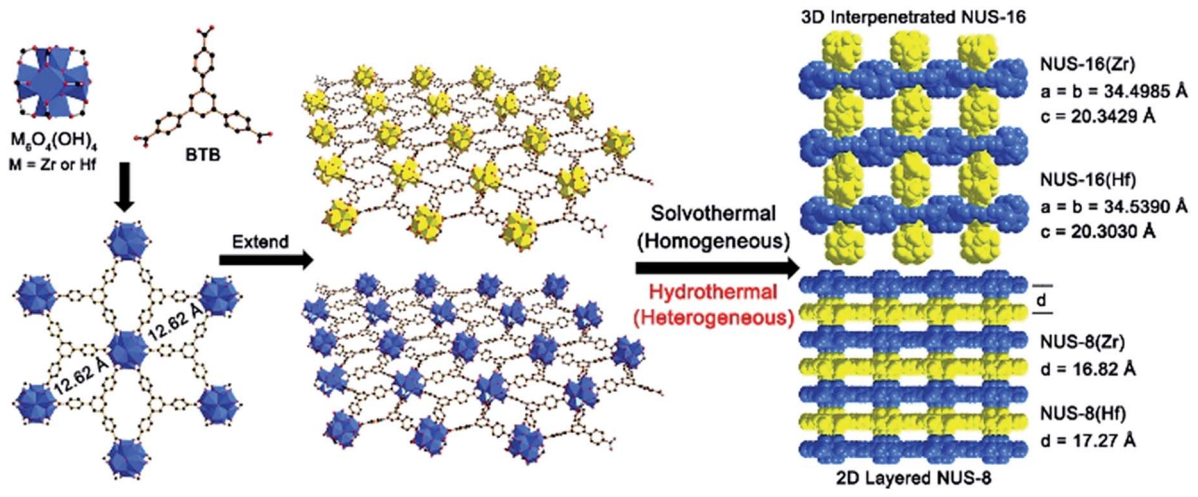

Fig. 1 Schematic illustration of the synthesis of 2D MOF nanosheets (NUS-8) and 3D interpenetrated MOFs (NUS-16) (M = Zr or Hf) using hydrothermal and solvothermal approaches, respectively. The homogeneous condition of solvothermal synthesis promotes the interpenetration of individual 2D nanosheets into a 3D network, while the heterogeneous condition of modulated hydrothermal synthesis prevents such interpenetration by fast precipitation of intermediate 2D MOF nanosheets.

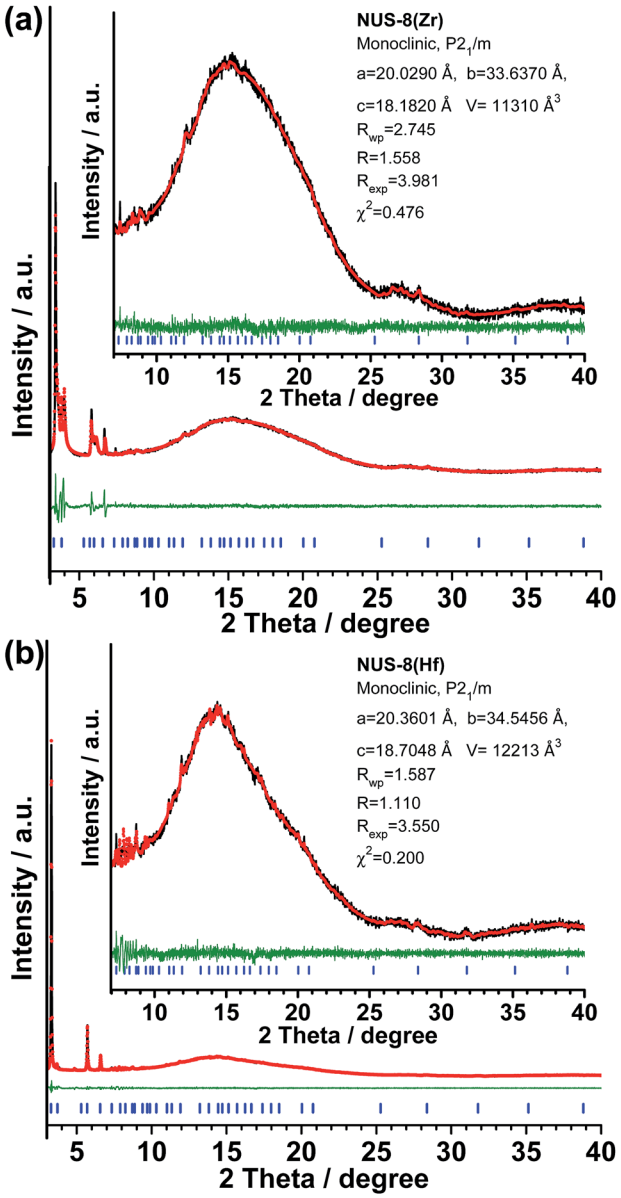

Fig. 2 Rietveld refinements of (a) NUS-8(Zr) and (b) NUS-8(Hf) based on synchrotron PXRD data from the LeBail route.

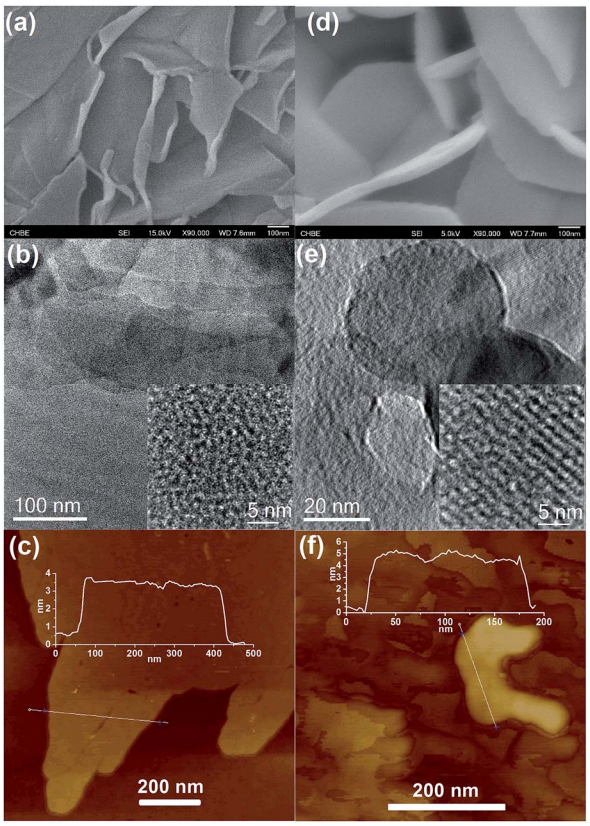

Fig. 3 Morphology characterization of NUS-8(Zr) (a–c) and NUS-8(Hf) (d–f) using FE-SEM (a, d), HR-TEM (b, e), and AFM (c, f).

a lateral size up to 500–1000 nm leading to high aspect ratios of 20–100 (Fig. 3a and d, S2†). The nanosheet morphology is a reflection of the 2D layered crystal structures of NUS-8, and can be attributed to the fast nucleation and precipitation under heterogeneous synthetic conditions.[40] The internal fine structures of NUS-8 crystals were investigated by high-resolution transmission electron microscopy (HR-TEM, Fig. 3b and e), wherein highly ordered crystalline domains could be found in NUS-8(Hf) with the lattice spacing of ~1 nm representing the (130) crystal plane. The nanosheet morphology of NUS-8 was confirmed by atomic force microscopy (AFM, Fig. 3c and f), wherein nanosheets as thin as ~3 nm for NUS-8(Zr) and ~4 nm for NUS-8(Hf) can be directly observed, suggesting merely two or three layers of stacking. These results have unambiguously proven the expected 2D layered structures and nanosheet morphology of NUS-8 MOFs, which can be attributed to the heterogeneous synthetic conditions capable of locking the MOF products in the kinetically favorable intermediate stage suitable for further gas sorption and catalysis applications.

Porosity evaluation

N_2 sorption isotherms collected at 77 K were used to evaluate the surface area and porosity of the obtained MOFs. As shown in Fig. 4a, both NUS-8(Zr) and NUS-8(Hf) exhibit hybrid Type I/IV N_2 sorption isotherms with noticeable hysteresis between adsorption and desorption branches, indicating their hybrid micro/meso-porous textures. The micropores (pore diameter less than 2 nm) can be justified from the crystal structures (Fig. 1), while the mesopores (pore diameter between 2 and 50 nm) may come from the interstitial voids of the irregular packing of nanosheets as seen from the FE-SEM images (Fig. 3a and d). In contrast, both NUS-16(Zr) and NUS-16(Hf) show Type I N_2 sorption isotherms, indicating their fully microporous structures induced by interpenetration.[37] NUS-8(Zr) has a Brunauer–Emmett–Teller (BET) surface area of 570 $m^2\ g^{-1}$ (Table S2†), which is lower than the reported value of collapsed 3D ZrBTB (613 $m^2\ g^{-1}$)[37] and 2D Hf-BTB metal–organic layers (661 $m^2\ g^{-1}$).[39] Normally, the introduction of heavier Hf cations will decrease the surface area because of increased crystal density.[41] However, compared to NUS-8(Zr), NUS-8(Hf) has a relatively high BET surface area of 628 $m^2\ g^{-1}$, probably because of the

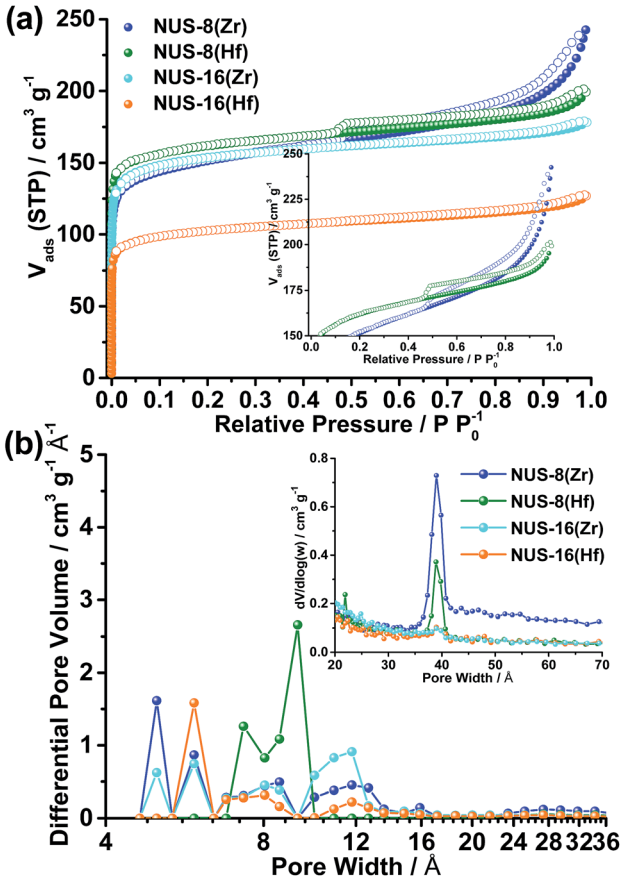

Fig. 4 (a) N_2 sorption isotherms at 77 K of NUS-8 and NUS-16 with inset featuring adsorption–desorption hysteresis; (b) pore size distribution of NUS-8 and NUS-16 calculated by NLDFT and BJH models (inset).

better crystallinity and less defects revealed by PXRD patterns.[42] In contrast, 3D interpenetrated NUS-16(Zr) and NUS-16(Hf) have decreased BET surface areas of 592 and 392 $m^2\ g^{-1}$, respectively, which can be attributed to the partial collapse of frameworks caused by the fragility of interpenetrated structures that will be discussed later.

The pore size distribution of NUS-8 calculated using non-local density functional theory (NLDFT) reveals two major pore sizes at ~6 and ~12 Å (Fig. 4b), which match well with the crystal structure (Fig. 1, 15.15 × 8.86 Å). Compared to NUS-8, NUS-16 has a reduced pore size of 10.72 × 8.12 Å, which is caused by the interpenetration of neighboring grids. Pore size distribution calculated using the Barrett–Joyner–Halenda (BJH) model suggests the existence of mesopores with pore sizes of ~3.9 nm for NUS-8 (Fig. 4b), agreeing well with the hybrid Type I/IV isotherms.

Stability tests

Several previous studies have indicated that MOFs with 3D interpenetrated structures should have larger surface areas than those with 2D layered structures due to the fully exposed edges and latent sides.[43] Our observation contradicts such conclusion, which prompts us to search other possible reasons. It has been reported that the stability of 3D interpenetrated ZrBTB [*aka* NUS-16(Zr) in this study] is much lower than that of other reported 3D Zr MOFs, which is attributed to the terminal H_2O and OH groups bound to fully exposed $Zr_6O_4(OH)_4$ clusters in ZrBTB as well as the reduced rigidity of the framework caused by interpenetration.[37] In the case of 2D layered NUS-8, however, the labile $Zr_6O_4(OH)_4$ clusters are shielded by interlayer packing leading to increased stability. In addition, the possible constraints caused by interpenetration in NUS-16 can be relieved in the 2D layered structure of NUS-8, which also helps to strengthen the framework stability. To fully unveil the superior stability of 2D NUS-8 MOFs over that of 3D NUS-16 MOFs, comprehensive stability tests were conducted, in which MOFs were treated with increased harshness of chemical exposure, from humid air, immersion in water, boiling in water, eventually to incubation in highly acidic solutions. The stability of treated MOFs was checked by PXRD and N_2 sorption experiments. In addition, thermogravimetric analyses (TGAs) were also conducted on pristine MOFs to evaluate their thermal stability. We found that 2D NUS-8 MOFs could retain their high structural integrity, almost intact porosity, and high decomposition temperatures up to 400 °C (Fig. S4†). More surprisingly, both NUS-8(Zr) and NUS-8(Hf) exhibit the highest 6A (boiling in water with retention of crystallinity and porosity) water stability;[44] and boiling in water does not affect their crystal structures and porosities. In contrast, 3D NUS-16 MOFs cannot survive in almost any of the tests as evidenced by the emergence of extra PXRD peaks, compromised PXRD peak intensity and Bragg peak broadening, reduced surface area, and continuous weight loss in TGA curves (Fig. S5†).[37] It is worth noting that for both NUS-8 and NUS-16, MOFs with Hf as the metal nodes tend to have higher stability than those with Zr ones. This can be explained by the higher bonding energy of Hf–O bonds (802 kJ mol^{-1}) than that of Zr–O bonds (776 kJ mol^{-1}).[45] In short, 2D NUS-8 MOFs possess higher chemical and thermal stability than that of 3D NUS-16 MOFs, which will surely pave the way toward their pragmatic applications under harsh conditions and at high temperatures.

Thermo-mechanical properties

We conducted dynamic mechanical analysis (DMA) experiments to further probe the reason of structural stability in 2D NUS-8 MOFs. Fig. 5 shows the storage moduli (E') and the loss moduli (E'') of the NUS-8 and NUS-16 MOFs, which are measures of the viscoelastic response as a function of temperature.[46,47] When subject to oscillatory stresses generated by a small strain deformation (Fig. 5a and b), the storage moduli data indicate that both NUS-16(Hf) and NUS-16(Zr) frameworks are thermo-mechanically stable with a stiffness value of *ca.* 10 GPa up to ~200 °C, but beyond which E' fell rapidly to under 1 GPa with elevated temperature. Up to ~280 °C, it appears that NUS-8(Hf) is relatively stable compared with NUS-16(Hf), which is consistent with TGA data (Fig. S4 and S5†). Notably, it can be seen in Fig. 5b that NUS-8(Zr) has, by and large, retained its initial storage modulus within the temperature range we studied (35–350 °C), whereas thermo-mechanical degradation was evidenced in the 3D interpenetrated counterpart NUS-16(Zr).

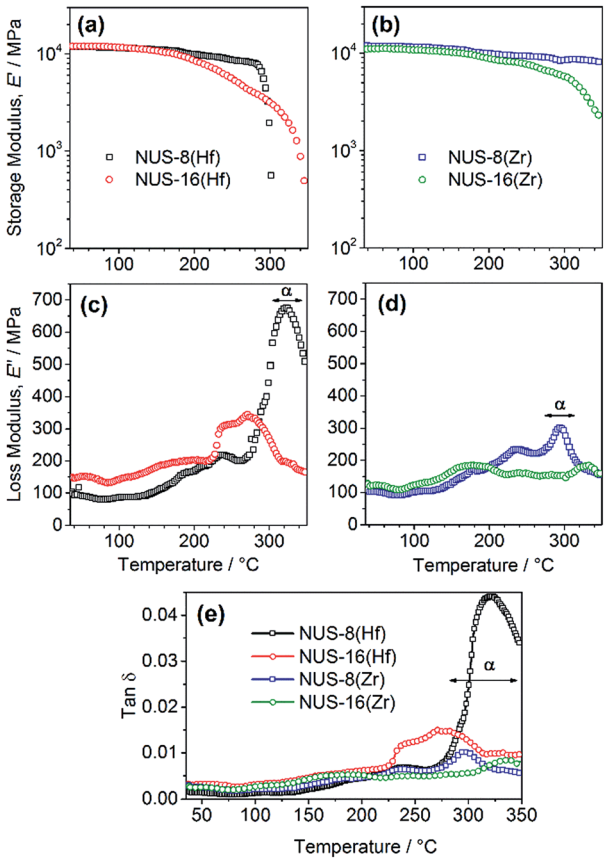

Fig. 5 Representative plots of DMA measurements: (a, b) storage modulus, E' and (c, d) loss modulus, E'', of NUS-8 and NUS-16. The primary relaxation is denoted as the α peak. (e) Loss tangent, tan $\delta = E''/E'$. All samples have been activated at 120 °C for 24 h under vacuum before being subjected to DMA studies.

The loss modulus, E'', represents the dissipative (lossy) component of the framework viscoelastic response in a dynamic stress state. The E'' data in Fig. 5c and d demonstrate that, because of the 2D configuration of the NUS-8 structures, thermo-mechanical dissipation is more substantial and may be arising from a combination of interlayer shear sliding deformation and out-of-plane tension/compression modes.[48] This effect is confirmed by the fact that the magnitudes of loss moduli of NUS-16 are appreciably lower, attributable to their interlocked 3D architecture which is tightly constrained (Fig. 1). Remarkably, we have established that between the 2D MOF nanosheets: NUS-8(Zr) is considerably less dissipative than NUS-8(Hf), evidenced from the loss tangent data (Fig. 5e) where the former framework is at least a factor of four times less lossy than that of the latter. We reasoned that this phenomenon may be linked to the much narrower 2D interlayer spacing of NUS-8(Zr) (d = 16.82 Å) compared with NUS-8(Hf) (17.27 Å), see Fig. 1.

Crystal growth mechanism studies of NUS-8

To disclose the crystal growth mechanism of 2D MOF nanosheets, we further carried out the reaction kinetics studies of NUS-8(Zr). PXRD and FESEM techniques were applied to monitor the crystal growth processes. As shown in Fig. 6a, the reaction intermediates after 1 h gave distinct XRD peaks similar to those of H_3BTB, suggesting the preservation of H_3BTB which is further confirmed by its FESEM images (pillar morphology, Fig. 6b). With the dissolution of H_3BTB and nucleation of NUS-8 planar crystallites, characteristic peaks featuring crystal planes (220) started to appear after 2 h and continued to grow with the time elapse, as evidenced by the continuous increase in PXRD peak intensity. FESEM images further support this claim. From 1 h to 2 h, the product morphology significantly changed from giant pillar (H_3BTB) to nanosheet [lateral size, $D_L \approx 1$ μm, NUS-8(Zr)]. With the time elapse, the nanosheets became larger and more uniform, with a continuous increase in lateral size from 1 μm (2 h) to larger than 3 μm (20 h). After 20 h, the product is mainly NUS-8(Zr) with uniform distribution of well-defined nanosheets and thickness ranging from 10 to 50 nm, matching well with the above observation of AFM images (Fig. 3c). These results clearly demonstrate the crystal growth mechanism in the modulated hydrothermal approach that the heterogeneous condition prevents interpenetration by fast precipitation of intermediate 2D MOF crystallites and promote further planar growth of NUS-8 nanosheets shown in Fig. 1.

Gas sorption properties

We further tested the CO_2 sorption property of NUS-8 MOFs.[49] Generally speaking, MOFs with exposed unsaturated metal centers (UMCs), exemplified by MOF-74 and HKUST-1,[50] can exhibit strong interactions with CO_2 affording high CO_2 uptake capacity and selectivity.[51] Considering the high density of Lewis acid sites and stability of 2D NUS-8 nanosheets, their adsorption-based CO_2 separation performance was thus evaluated.[52,53] NUS-8(Zr) has a slightly lower CO_2 working capacity (15% CO_2 content for post-combustion CO_2 capture) than that of NUS-8(Hf) (0.30 mmol g^{-1} *vs.* 0.31 mmol g^{-1}, Fig. 7a, S6, S7 & Table S2†). This performance is comparable to that of UiO-66(Zr) (0.37 mmol g^{-1}),[41] albeit a much lower BET surface area of NUS-8(Zr) (570 m^2 g^{-1} *vs.* 1500 m^2 g^{-1}). This can be attributed to the smaller pore size (Fig. 4b) and stronger Lewis acidity of NUS-8(Zr).[54] Meanwhile, both NUS-8(Zr) and NUS-8(Hf) have much higher CO_2 working capacities than that of NUS-16(Zr) (0.18 mmol g^{-1}) and NUS-16(Hf) (0.22 mmol g^{-1}), which can be attributed to the reduced BET surface areas caused by framework collapse of NUS-16 MOFs.

The stronger interactions between NUS-8(Zr) and CO_2 can be verified by comparing the isosteric heat of adsorption (Q_{st}) of CO_2 (Fig. 7b & Table S3†).[55] The zero-coverage Q_{st} of CO_2 in NUS-8(Zr) (26.5 kJ mol^{-1}) is indeed higher than that in NUS-8(Hf) (21.2 kJ mol^{-1}) and UiO-66(Zr) (25 kJ mol^{-1}).[41,56] This is also confirmed in 3D NUS-16, wherein NUS-16(Zr) has a higher CO_2 Q_{st} than that of NUS-16(Hf) (23.0 kJ mol^{-1} *vs.* 20.5 kJ mol^{-1}). The above result is consistent with the fact that $Zr_6O_4(OH)_4$ clusters have stronger Lewis acidity than that of Hf_6 clusters due to the smaller cation radius of Zr over Hf.[57] The CO_2/N_2 and CO_2/CH_4 adsorptive selectivities of NUS-8 MOFs were further evaluated using ideal adsorption solution theory (IAST).[58] Similar to the trend of Q_{st}, NUS-8(Zr) also has a higher IAST CO_2/

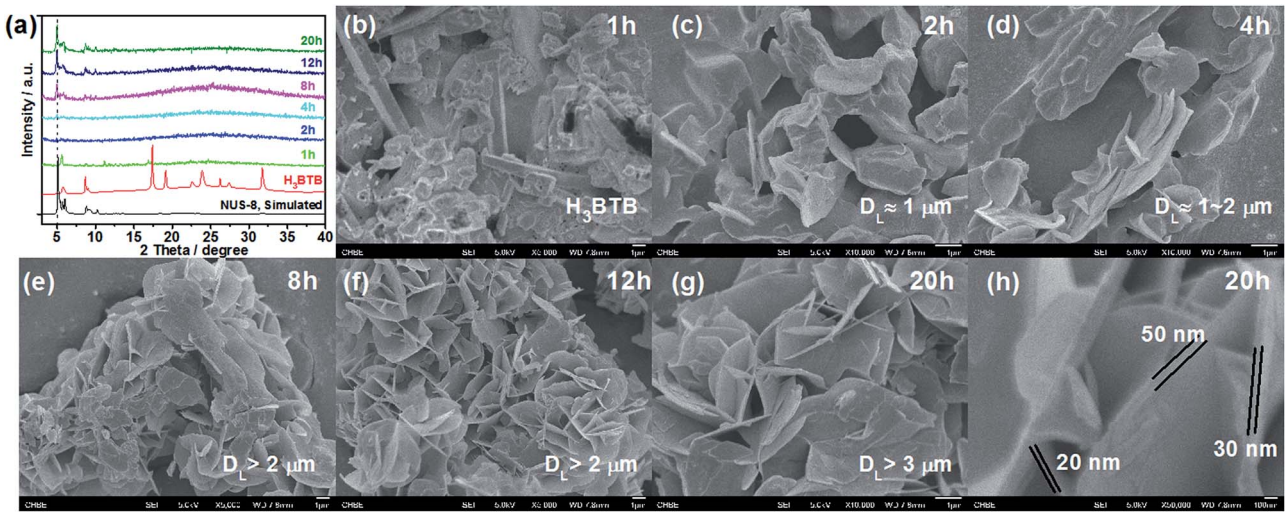

Fig. 6 Crystal growth mechanism studies of NUS-8(Zr): (a) PXRD patterns; (b–h) FESEM images at different reaction times.

N_2 (14) and CO_2/CH_4 (5.6) selectivities than those of NUS-8(Hf) (11 & 3.9, Table S3†), again confirming the importance of strong interactions between CO_2 and MOF adsorbents.

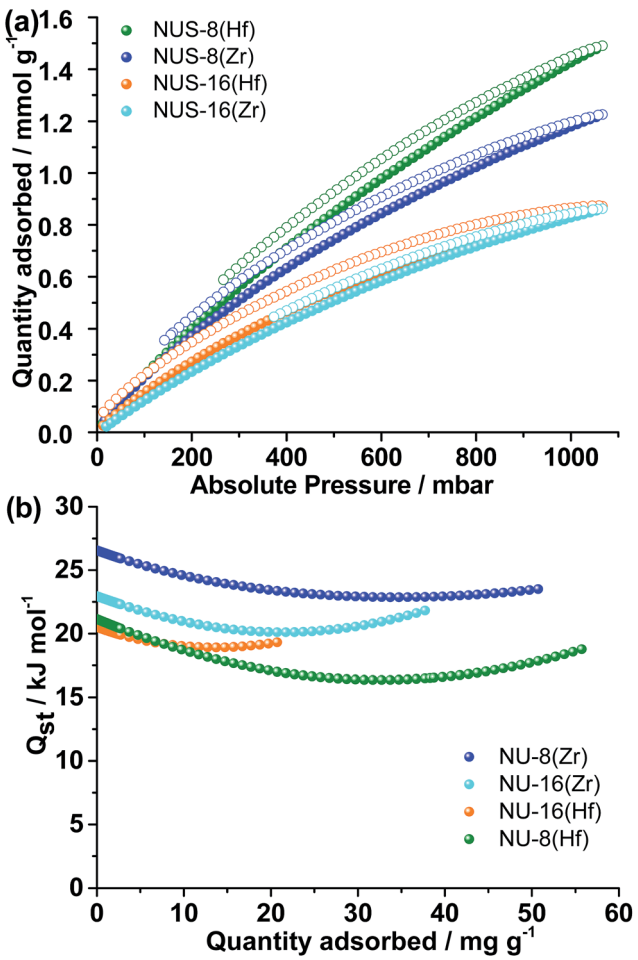

Fig. 7 (a) CO_2 sorption isotherms of NUS-8 and NUS-16 at 298 K; (b) Q_{st} of CO_2 in NUS-8 and NUS-16.

Catalytic oxidation of thioethers

As revealed by NUS-8 crystal models, the coordinatively unsaturated Zr/Hf sites in the 12-connected M_6 clusters may serve as Lewis acid sites.[59–61] Therefore, the relatively large pore size and immense in-plane surface area should be highly beneficial for heterogeneous catalysis due to the highly accessible Lewis acid sites and enhanced mass transfer, as has been suggested in porous MOFs and zeolites.[62] This hybrid porosity, high stability, and immense Lewis acid sites have encouraged us to investigate the catalytic performance of 2D NUS-8 nanosheets. The catalytic performance of NUS-8 and NUS-16 was evaluated based on the oxidation reaction of thioethers into sulfoxides and sulfones, which is an important reaction due to its versatile utility in organic synthesis.[63] In this study, thioether oxidation reactions were conducted in the presence of 30% H_2O_2 using MOFs as the catalysts to produce the corresponding oxygenated products (sulfoxides, $PhSOCH_3$ and sulfones, $PhSO_2CH_3$) in quantitative yield based on the consumption of H_2O_2 and thioanisole (Table 1).[64]

We initially attempted this reaction using NUS-8(Zr) as the catalyst and acetonitrile (CH_3CN) as the solvent.[64] In the absence of catalyst, thioanisole can hardly be oxidized by 30% H_2O_2 at ambient temperatures (only 12% conversion). When using NUS-8(Zr) as the catalyst, we obtained a thioanisole conversion of 100% and $PhSO_2CH_3$ selectivity of 94.3% (Table 1), which is higher than that of the Zr cluster based poly(-polyoxotungstate) catalyst with 84% $PhSO_2CH_3$ selectivity at a higher temperature (60 °C).[65]

Among all the solvents, reactions conducted in dichloromethane (DCM) have the highest $PhSO_2CH_3$ selectivity (~100%) at room temperature. Therefore, DCM was chosen as the solvent for further optimization. To the best of our knowledge, this high conversion and sulfone selectivity are rarely reported in the literature, especially for MOF catalysts.[66,67] Interestingly, reactions conducted using THF as the solvent exhibit a decreased conversion (74%), possibly due to the strong binding of THF to the Lewis acid sites of MOFs.[68] Either increasing the loading of

Table 1 Screening the best conditions for thioanisole oxidation in the presence of 30% H_2O_2 catalyzed by NUS-8(Zr) at 298 K

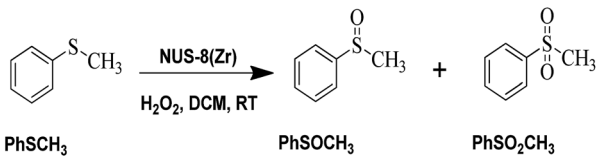

Entry	Catalyst loading (mol%)	Time (h)	Conv. (%)	Selectivity (%)	
				$PhSOCH_3$	$PhSO_2CH_3$
CH_3CN	0	1	12	100	0
CH_3CN	3.5	1	>99	5.7	94.3
H_2O	3.5	1	>99	33.3	66.7
CH_3OH	3.5	1	>99	1.2	98.8
THF	3.5	1	74	7.3	92.7
DCM	3.5	1	>99	0	100
DCM	3.5	0.5	87	0	100
DCM	3.5	1.5	>99	0	100
DCM	0	1	8	100	0
DCM	5	1	>99	0	100
DCM	2.1	1	>99	0	100
DCM	1.5	1	>99	0	100
DCM	1.25	1	96	1.7	98.3

NUS-8(Zr) to 5 mol% or decreasing to 1.5 mol% did not affect the conversion and sulfone selectivity. However, further decreasing the catalyst loading to 1.25 mol% led to a lower conversion (96%) and reduced sulfone selectivity (98.3%), possibly due to insufficient catalysis (Table 1). A control experiment without any catalyst in DCM afforded less than 8% conversion, confirming the critical role of NUS-8(Zr) as the catalyst in this reaction. When NUS-8(Hf) was used as the catalyst under a similar reaction condition, a conversion of 88% for thioanisole was obtained along with a high sulfone selectivity (89%) (Fig. 8b). This performance is inferior to that of NUS-8(Zr), but is still comparable to the Zr_{24}-cluster based poly(polyoxotungstate) catalyst (84% $PhSO_2CH_3$ selectivity).[65]

Following these results, we then examined the heterogeneity and recyclability of NUS-8 catalysts. The supernatant of the reaction media obtained by using a regular filter during the oxidation reaction did not yield any additional product, indicating the role of the heterogeneous catalyst played by NUS-8 nanosheets (Fig. 8a). Upon completion of the reaction, NUS-8(Zr) could be recovered in a quantitative yield and used repeatedly without significant loss of catalytic activity for subsequent three runs (Fig. 8c, constant 100% conversion and 100% selectivity for further 1–3 runs, respectively). This was also observed in NUS-8(Hf) (Fig. 8c, constant 88% conversion and 87% selectivity for further 1–3 runs, respectively). Recycled NUS-8 nanosheets retained high crystallinity (Fig. S8†), intact morphology (Fig. S10 and S11†), but with mildly reduced porosity (Fig. S9†), possibly due to the trapping of reagents in the frameworks that are hard to be removed during mild regeneration processes. It was further confirmed by elementary analysis (EA) results (Table S4†) that the C/Zr or C/Hf ratio in NUS-8 nanosheets remained almost intact [0.87 to

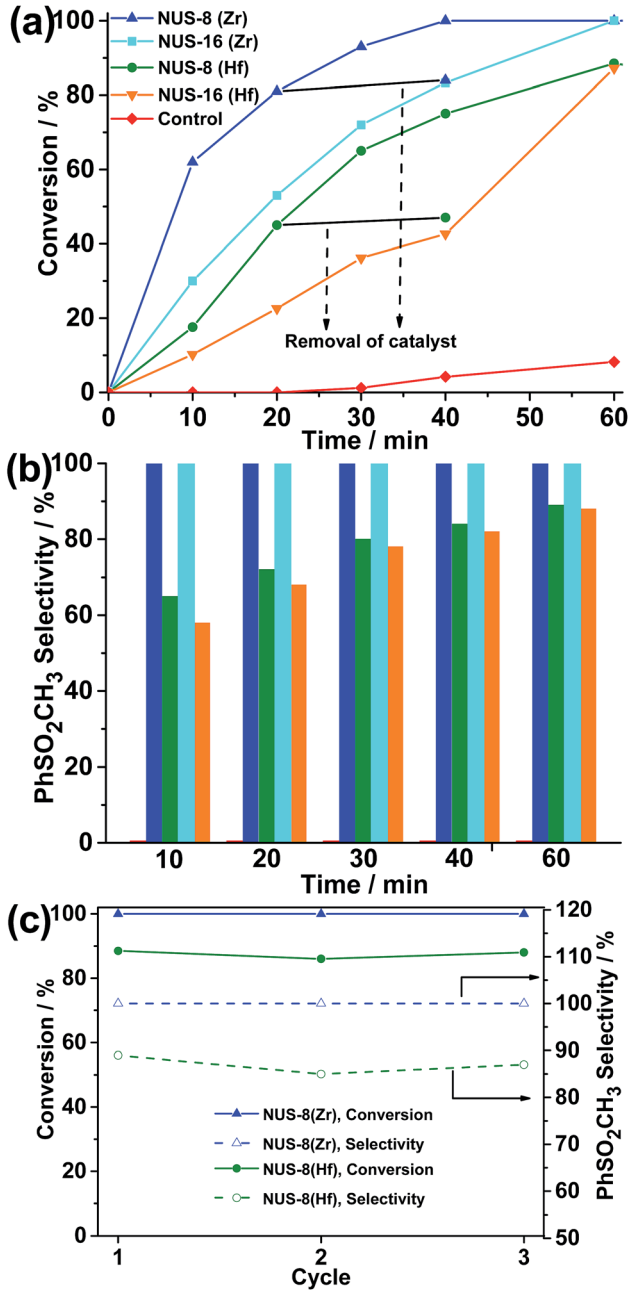

Fig. 8 Kinetic study of thioanisole oxidation catalyzed by NUS-8 or NUS-16 at room temperature: (a) kinetic studies; (b) $PhSO_2CH_3$ selectivity *versus* time; (c) cycle performance.

0.83 for NUS-8(Zr); 1.65 to 1.62 for NUS-8(Hf)] after three catalytic runs.

To further probe the superior catalytic activity of 2D NUS-8 nanosheets over 3D NUS-16 bulk crystals, we conducted kinetic studies of this reaction using 1.5 mol% loading of catalysts at 298 K for a continuous period of one hour (Fig. 8a and b). A negligible conversion (~0%) within 20 min was observed without any catalyst. In contrast, reactions catalyzed by either NUS-8 or NUS-16 displayed remarkably enhanced conversion and sulfone selectivity, with continuous increase in both conversion and sulfone selectivity within one hour. The

faster reaction kinetics in the presence of MOFs can be explained by the strong Lewis acidity of Zr/Hf MOFs.[59,69] Reactions catalyzed by NUS-8 demonstrated faster kinetics than those catalyzed by NUS-16, which can be attributed to the 2D nature of NUS-8 facilitating the diffusion of substrates and products near the active sites.[70] In addition, Zr-based MOFs tend to afford faster reaction kinetics and higher sulfone selectivity than Hf-based ones under the same reaction conditions, which can be attributed to the stronger Lewis acidity of Zr^{4+} than Hf^{4+}.[71]

Assessment of Lewis acidity

In this study, NH_3 temperature program desorption (TPD) was conducted to compare the strength of Lewis acidity of MOFs and explain why 2D NUS-8 MOFs have better catalytic activity than 3D NUS-16 ones.[72] Before TPD tests, the sample was charged into a quartz tube and then activated in a helium flow at 150 °C for 2 h. The sample was subsequently exposed to pure NH_3 gas (30 mL min^{-1}) for 30 minutes and then purged with helium flow at 100 °C for 2 h. The temperature was increased to 450 °C at a ramping rate of 5 °C min^{-1}, and the desorbed NH_3 was detected using a TCD detector. As depicted in Fig. 9, NH_3 desorption peaks at higher temperatures indicate stronger acidity, while the appearance of two or more peaks indicates multiple acid sites (from strong to weak). NUS-8(Zr) shows the highest strength of strong acidity (single desorption peak at ~400 °C), which is consistent with the catalytic performance revealed above. Unlike NUS-8(Zr), NUS-8(Hf) exhibits two major desorption peaks at 300 and 425 °C, which can be assigned to two acidic sites (weak and strong). This can possibly explain why NUS-8(Hf) shows a constant 12% sulfoxide and 88% sulfone selectivity. However, neither NUS-16(Zr) nor NUS-16(Hf) (thermally unstable, Fig. S5†) could survive from the NH_3-TPD experimental conditions (adsorption and desorption at high temperature), accompanied by negligible desorption peaks (Fig. 9). The NH_3-TPD results shown herein suggest that: (1) the higher catalytic performance of NUS-8(Zr) over NUS-8(Hf) is because of the stronger acidity; (2) 2D NUS-8 nanosheets have a higher stability than 3D NUS-16, which is also supported by the stability tests shown in Fig. S4 and S5;† (3) the catalytic selectivity can be tuned *via* the introduction of multi-sites in MOFs exemplified by NUS-8(Hf).

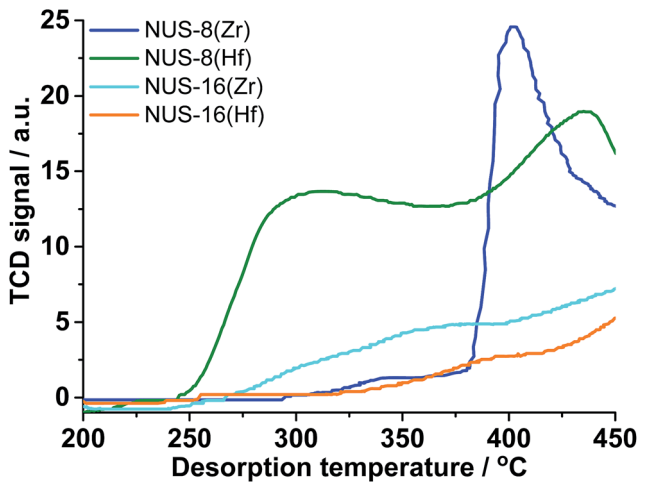

Fig. 9 Acidity strength in NUS-8 and NUS-16 revealed by NH_3 temperature-programmed desorption (TPD).

Conclusions

In conclusion, we have described a bottom-up strategy to synthesize 2D MOF nanosheets directly *via* a heterogeneous modulated hydrothermal approach in the absence of surfactants. Structural refinements of synchrotron PXRD data indicate the 2D planar structure of NUS-8 formed by inhibition of interpenetration. 2D NUS-8 nanosheets exhibit excellent stabilities superior to that of their interlocked 3D MOF analogues (NUS-16) synthesized solvothermally, which are evidenced by comprehensive stability tests. Dynamic mechanical analysis (DMA) experiments suggest that the stability may come from a combination of interlayer shear sliding deformation and out-of-plane tension/compression modes whereas their interlocked 3D architecture is confined. Both NUS-8 and NUS-16 were used as Lewis acid catalysts for the oxidation reactions of thioanisole into sulfones, in which 2D NUS-8 nanosheets exhibited better reaction kinetics and sulfone selectivity than 3D NUS-16. In addition, NUS-8(Zr) showed superior reaction kinetics with 100% conversion and 100% sulfone selectivity even at ambient temperatures, which can be attributed to its strong Lewis acidity as evidenced by stronger CO_2 affinity and superior acidity observed in NH_3-TPD experiments. Our work has demonstrated the potential of the modulated hydrothermal approach in the kinetically controlled synthesis of 2D MOF nanosheets and offered another versatile approach for the synthesis and structure/morphology control of these promising materials.

Acknowledgements

This work is supported by National University of Singapore (CENGas R-261-508-001-646) and Ministry of Education – Singapore (MOE AcRF Tier 2 R-279-000-429-112).

Notes and references

1 K. S. Novoselov, A. K. Geim, S. V. Morozov, D. Jiang, Y. Zhang, S. V. Dubonos, I. V. Grigorieva and A. A. Firsov, *Science*, 2004, **306**, 666–669.
2 B. Dubertret, T. Heine and M. Terrones, *Acc. Chem. Res.*, 2015, **48**, 1–2.
3 A. P. Côté, A. I. Benin, N. W. Ockwig, M. O'Keeffe, A. J. Matzger and O. M. Yaghi, *Science*, 2005, **310**, 1166–1170.
4 G. R. Bhimanapati, Z. Lin, V. Meunier, Y. Jung, J. Cha, S. Das, D. Xiao, Y. Son, M. S. Strano, V. R. Cooper, L. Liang, S. G. Louie, E. Ringe, W. Zhou, S. S. Kim, R. R. Naik, B. G. Sumpter, H. Terrones, F. Xia, Y. Wang, J. Zhu, D. Akinwande, N. Alem, J. A. Schuller, R. E. Schaak, M. Terrones and J. A. Robinson, *ACS Nano*, 2015, **9**, 11509–11539.

5 X. Ling, Y. Lin, Q. Ma, Z. Wang, Y. Song, L. Yu, S. Huang, W. Fang, X. Zhang, A. L. Hsu, Y. Bie, Y.-H. Lee, Y. Zhu, L. Wu, J. Li, P. Jarillo-Herrero, M. Dresselhaus, T. Palacios and J. Kong, *Adv. Mater.*, 2016, **28**, 2322–2329.
6 S. Z. Butler, S. M. Hollen, L. Cao, Y. Cui, J. A. Gupta, H. R. Gutiérrez, T. F. Heinz, S. S. Hong, J. Huang, A. F. Ismach, E. Johnston-Halperin, M. Kuno, V. V. Plashnitsa, R. D. Robinson, R. S. Ruoff, S. Salahuddin, J. Shan, L. Shi, M. G. Spencer, M. Terrones, W. Windl and J. E. Goldberger, *ACS Nano*, 2013, **7**, 2898–2926.
7 S. Jeong, D. Yoo, M. Ahn, P. Miró, T. Heine and J. Cheon, *Nat. Commun.*, 2015, **6**, 5763.
8 G. Férey, *Chem. Soc. Rev.*, 2008, **37**, 191–214.
9 H. C. Zhou, J. R. Long and O. M. Yaghi, *Chem. Rev.*, 2012, **112**, 673–674.
10 W. Xuan, C. Zhu, Y. Liu and Y. Cui, *Chem. Soc. Rev.*, 2012, **41**, 1677–1695.
11 H. Furukawa, K. E. Cordova, M. O'Keeffe and O. M. Yaghi, *Science*, 2013, **341**, 1230444.
12 H.-C. Zhou and S. Kitagawa, *Chem. Soc. Rev.*, 2014, **43**, 5415–5418.
13 Y. Cui, B. Li, H. He, W. Zhou, B. Chen and G. Qian, *Acc. Chem. Res.*, 2016, **49**, 483–493.
14 G. Liu, Y. Wang, C. Shen, Z. Ju and D. Yuan, *J. Mater. Chem. A*, 2015, **3**, 3051–3058.
15 H. Zhang, *ACS Nano*, 2015, **9**, 9451–9469.
16 B. Li, K. Leng, Y. Zhang, J. J. Dynes, J. Wang, Y. Hu, D. Ma, Z. Shi, L. Zhu, D. Zhang, Y. Sun, M. Chrzanowski and S. Ma, *J. Am. Chem. Soc.*, 2015, **137**, 4243–4248.
17 Y. Peng, Y. Li, Y. Ban, H. Jin, W. Jiao, X. Liu and W. Yang, *Science*, 2014, **346**, 1356–1359.
18 J.-C. Tan, P. J. Saines, E. G. Bithell and A. K. Cheetham, *ACS Nano*, 2012, **6**, 615–621.
19 C. Hermosa, B. R. Horrocks, J. I. Martinez, F. Liscio, J. Gomez-Herrero and F. Zamora, *Chem. Sci.*, 2015, **6**, 2553–2558.
20 P.-Z. Li, Y. Maeda and Q. Xu, *Chem. Commun.*, 2011, **47**, 8436–8438.
21 M. Osada and T. Sasaki, *Adv. Mater.*, 2012, **24**, 210–228.
22 M. O'Keeffe and O. M. Yaghi, *Chem. Rev.*, 2012, **112**, 675–702.
23 S. C. Junggeburth, L. Diehl, S. Werner, V. Duppel, W. Sigle and B. V. Lotsch, *J. Am. Chem. Soc.*, 2013, **135**, 6157–6164.
24 M. Zhao, Y. Wang, Q. Ma, Y. Huang, X. Zhang, J. Ping, Z. Zhang, Q. Lu, Y. Yu, H. Xu, Y. Zhao and H. Zhang, *Adv. Mater.*, 2015, **27**, 7372–7378.
25 Y. Wang, M. Zhao, J. Ping, B. Chen, X. Cao, Y. Huang, C. Tan, Q. Ma, S. Wu, Y. Yu, Q. Lu, J. Chen, W. Zhao, Y. Ying and H. Zhang, *Adv. Mater.*, 2016, **28**, 4149–4155.
26 A. Rabenau, *Angew. Chem., Int. Ed.*, 1985, **24**, 1026–1040.
27 G. Férey, C. Mellot-Draznieks, C. Serre, F. Millange, J. Dutour, S. Surblé and I. Margiolaki, *Science*, 2005, **309**, 2040–2042.
28 L. Hamon, C. Serre, T. Devic, T. Loiseau, F. Millange, G. Ferey and G. De Weireld, *J. Am. Chem. Soc.*, 2009, **131**, 8775–8777.
29 J. W. Yoon, H. Chang, S.-J. Lee, Y. K. Hwang, D.-Y. Hong, S.-K. Lee, J. S. Lee, S. Jang, T.-U. Yoon, K. Kwac, Y. Jung, R. S. Pillai, F. Faucher, A. Vimont, M. Daturi, G. Ferey, C. Serre, G. Maurin, Y.-S. Bae and J.-S. Chang, *Nat. Mater.*, 2017, DOI: 10.1038/nmat4825.
30 J. Shen, Y. Zhu, H. Jiang and C. Li, *Nano Today*, 2016, **11**, 483–520.
31 B. Seoane, S. Castellanos, A. Dikhtiarenko, F. Kapteijn and J. Gascon, *Coord. Chem. Rev.*, 2016, **307**, 147–187.
32 S. M. Cohen, *J. Am. Chem. Soc.*, 2017, **139**, 2855–2863.
33 A. J. Howarth, A. W. Peters, N. A. Vermeulen, T. C. Wang, J. T. Hupp and O. K. Farha, *Chem. Mater.*, 2017, **29**, 26–39.
34 Z. Hu, Y. Peng, Z. Kang, Y. Qian and D. Zhao, *Inorg. Chem.*, 2015, **54**, 4862–4868.
35 Z. Hu, A. Nalaparaju, Y. Peng, J. Jiang and D. Zhao, *Inorg. Chem.*, 2016, **55**, 1134–1141.
36 Z. Hu and D. Zhao, *Dalton Trans.*, 2015, **44**, 19018–19040.
37 R. Wang, Z. Wang, Y. Xu, F. Dai, L. Zhang and D. Sun, *Inorg. Chem.*, 2014, **53**, 7086–7088.
38 O. Shekhah, H. Wang, M. Paradinas, C. Ocal, B. Schüpbach, A. Terfort, D. Zacher, R. A. Fischer and C. Wöll, *Nat. Mater.*, 2009, **8**, 481–484.
39 L. Cao, Z. Lin, F. Peng, W. Wang, R. Huang, C. Wang, J. Yan, J. Liang, Z. Zhang, T. Zhang, L. Long, J. Sun and W. Lin, *Angew. Chem., Int. Ed.*, 2016, **55**, 4962–4966.
40 Z. Hu, M. Khurana, Y. H. Seah, M. Zhang, Z. Guo and D. Zhao, *Chem. Eng. Sci.*, 2015, **124**, 61–69.
41 Z. Hu, K. Zhang, M. Zhang, Z. Guo, J. Jiang and D. Zhao, *ChemSusChem*, 2014, **7**, 2791–2795.
42 Z. Hu, I. Castano, S. Wang, Y. Wang, Y. Peng, Y. Qian, C. Chi, X. Wang and D. Zhao, *Cryst. Growth Des.*, 2016, **16**, 2295–2301.
43 P. Nugent, Y. Belmabkhout, S. D. Burd, A. J. Cairns, R. Luebke, K. Forrest, T. Pham, S. Q. Ma, B. Space, L. Wojtas, M. Eddaoudi and M. J. Zaworotko, *Nature*, 2013, **495**, 80–84.
44 B. S. Gelfand and G. K. H. Shimizu, *Dalton Trans.*, 2016, **45**, 3668–3678.
45 M. H. Beyzavi, R. C. Klet, S. Tussupbayev, J. Borycz, N. A. Vermeulen, C. J. Cramer, J. F. Stoddart, J. T. Hupp and O. K. Farha, *J. Am. Chem. Soc.*, 2014, **136**, 15861–15864.
46 E. M. Mahdi and J.-C. Tan, *Polymer*, 2016, **97**, 31–43.
47 E. M. Mahdi and J.-C. Tan, *J. Membr. Sci.*, 2016, **498**, 276–290.
48 M. Zhang, G. Feng, Z. Song, Y.-P. Zhou, H.-Y. Chao, D. Yuan, T. T. Y. Tan, Z. Guo, Z. Hu, B. Z. Tang, B. Liu and D. Zhao, *J. Am. Chem. Soc.*, 2014, **136**, 7241–7244.
49 X. Q. Kong, E. Scott, W. Ding, J. A. Mason, J. R. Long and J. A. Reimer, *J. Am. Chem. Soc.*, 2012, **134**, 14341–14344.
50 P. M. Forster, J. Eckert, B. D. Heiken, J. B. Parise, J. W. Yoon, S. H. Jhung, J. S. Chang and A. K. Cheetham, *J. Am. Chem. Soc.*, 2006, **128**, 16846–16850.
51 T. H. Bae, M. R. Hudson, J. A. Mason, W. L. Queen, J. J. Dutton, K. Sumida, K. J. Micklash, S. S. Kaye, C. M. Brown and J. R. Long, *Energy Environ. Sci.*, 2013, **6**, 128–138.

52 S. S. Myers, A. Zanobetti, I. Kloog, P. Huybers, A. D. Leakey, A. J. Bloom, E. Carlisle, L. H. Dietterich, G. Fitzgerald and T. Hasegawa, *Nature*, 2014, **510**, 139–142.
53 K. Sumida, D. L. Rogow, J. A. Mason, T. M. McDonald, E. D. Bloch, Z. R. Herm, T. H. Bae and J. R. Long, *Chem. Rev.*, 2012, **112**, 724–781.
54 Z. G. Hu, S. Faucher, Y. Y. Zhuo, Y. Sun, S. N. Wang and D. Zhao, *Chem.–Eur. J.*, 2015, **21**, 17246–17255.
55 J. L. C. Rowsell and O. M. Yaghi, *J. Am. Chem. Soc.*, 2006, **128**, 1304–1315.
56 G. E. Cmarik, M. Kim, S. M. Cohen and K. S. Walton, *Langmuir*, 2012, **28**, 15606–15613.
57 S. Y. Moon, Y. Y. Liu, J. T. Hupp and O. K. Farha, *Angew. Chem., Int. Ed.*, 2015, **54**, 6795–6799.
58 A. L. Myers and J. M. Prausnitz, *AIChE J.*, 1965, **11**, 121–127.
59 S. Horike, M. Dincă, K. Tamaki and J. R. Long, *J. Am. Chem. Soc.*, 2008, **130**, 5854–5855.
60 Z. Hu and D. Zhao, *CrystEngComm*, 2017, DOI: 10.1039/c1036ce02660e.
61 Z. Hu, Y. Peng, Y. Gao, Y. Qian, S. Ying, D. Yuan, S. Horike, N. Ogiwara, R. Babarao, Y. Wang, N. Yan and D. Zhao, *Chem. Mater.*, 2016, **28**, 2659–2667.
62 S. Mitchell, A. B. Pinar, J. Kenvin, P. Crivelli, J. Kärger and J. Pérez-Ramírez, *Nat. Commun.*, 2015, **6**, 8633.
63 I. Fernández and N. Khiar, *Chem. Rev.*, 2003, **103**, 3651–3706.
64 O. A. Kholdeeva, G. M. Maksimov, R. I. Maksimovskaya, L. A. Kovaleva, M. A. Fedotov, V. A. Grigoriev and C. L. Hill, *Inorg. Chem.*, 2000, **39**, 3828–3837.
65 L. Huang, S.-S. Wang, J.-W. Zhao, L. Cheng and G.-Y. Yang, *J. Am. Chem. Soc.*, 2014, **136**, 7637–7642.
66 J. Liu, L. Chen, H. Cui, J. Zhang, L. Zhang and C.-Y. Su, *Chem. Soc. Rev.*, 2014, **43**, 6011–6061.
67 A. Corma, H. Garcia and F. X. L. Xamena, *Chem. Rev.*, 2010, **110**, 4606–4655.
68 R. Q. Zou, H. Sakurai, S. Han, R. Q. Zhong and Q. Xu, *J. Am. Chem. Soc.*, 2007, **129**, 8402–8403.
69 Z. Hu, Y. Peng, K. M. Tan and D. Zhao, *CrystEngComm*, 2015, **17**, 7124–7129.
70 R. Krishna, *J. Phys. Chem. C*, 2009, **113**, 19756–19781.
71 C. Housecroft and A. G. Sharpe, *Inorganic Chemistry*, Prentice Hall, 2012.
72 J. Jiang and O. M. Yaghi, *Chem. Rev.*, 2015, **115**, 6966–6997.

